

METHODOLOGIES TO PREDICT HYDRODYNAMIC CHARACTERISTICS OF PUSHER AND PULLER PODDED PROPULSORS IN OBLIQUE FLOWS

(DOI No: 10.3940/rina.ijme.2016.a4.376)

M F Islam, Oceanic Consulting Corporation, Canada, F Jahra, Fleetway Inc.

SUMMARY

This paper presents the outcome of a numerical simulation based research program to evaluate the propulsive characteristics of puller and pusher podded propulsors in a straight course and at static azimuthing conditions while operating in open water. Methodologies to predict the propeller thrust and torque, and pod forces and moments in three dimensions using a Reynolds-Averaged Navier Stokes (RANS) solver at multiple azimuthing conditions and pod configurations are presented. To obtain insight into the reliability and accuracy of the results, grid and time step dependency studies are conducted for a podded propulsor in straight-ahead condition. The simulation techniques and results are first validated against measurements of a bare propeller and a podded propulsor in straight ahead condition for multiple loading scenarios and in both puller and pusher configurations. Next, simulations were carried out to model the podded propulsors in the two configurations at multiple loading conditions and at various azimuthing angles from $+30^\circ$ to -30° in 15° increments. The majority of the simulations are carried out using both steady state and unsteady state conditions, primarily to evaluate the effect of setup conditions on the computation time and prediction accuracy. The predicted performance characteristics of the pod unit using the unsteady RANS method were within 1% to 5% of the corresponding experimental measurements for all the loading conditions, azimuthing angles and pod configurations studied. The non-linear behaviour of the performance coefficients of the pod unit are well captured at various loading and azimuthing conditions in the predicted results. This study demonstrates that the RANS solver, with proper meshing arrangement, boundary conditions and setup techniques can predict the performance characteristics of the podded propulsor in multiple azimuthing angles, pod configurations and in the various loading conditions with a same level of accuracy as experimental results. Additionally, the velocity and pressure distributions on and around the pod-strut-propeller bodies are discussed as derived from the RANS predictions.

1. INTRODUCTION

Podded propulsors are widely used in the marine industry and are becoming more popular, not only for passenger ships, but also for offshore drilling units, offshore supply vessels, tugs, ice breakers and naval vessels. They allow more flexibility in the design of the internal arrangement of a ship, potentially reduced noise and vibration, and increased manoeuvrability, [1] and [2]. Two types of pod configurations are primarily used in the marine industry. In the puller type, the propeller is located upstream of the pod and strut but in the pusher type the propeller is downward of the pod and strut [3].

One of the most attractive features of a podded propulsor is its ability to direct its thrust toward any direction in a 360° horizon. However, this feature also brought a number of concerns such as the nature of forces and moments on the unit that result from the hydrodynamic interaction between its components at different loading conditions. Bearing forces, steering moments and transverse force are particularly important in conditions such as manoeuvring, turns at high speed and sailing in a seaway. Failures on early units led to a study about the sources of failure of podded propulsors [1 and 2]. These studies showed that bearings and seals were the sources of over one-half of the failures, thus highlighting the importance of predicting bearing and other propulsion forces accurately. Moreover, the propeller forces and moments are by no means steady and important contributions to the vibration excitation may arise

from the propeller working in a far from uniform hull wake. A thorough investigation of the hydrodynamics behind the fluctuation of these forces and moments while operating in straight course and azimuthing conditions is required for a proper understanding of the issue. There are a few recently published works that address the behavior of podded propulsors at static and dynamic azimuthing angles: Szantyr ([4],[5]), Grygorowicz and Szantyr [6], Woodward et al. [7], Heinke [8], Stettler [9], Reichel [10], Wang [11], Islam et al. [12], Akinturk et al. [13], Liu et al. [14] are the most relevant ones.

The performance prediction of marine propellers is often considered as one of the most challenging tasks in marine hydrodynamics due to the complexity of propeller geometry which generates strong rotational flows, with 3D boundary layers, strongly anisotropic structure of turbulence, high pressure gradients and fluid acceleration. For podded propulsors, an additional complexity is expected due to the strong interaction between the rotating part (propeller) and the fixed parts (pod and strut), especially at high azimuth (yaw) angles. Due to the complexity of the system, expensive and time consuming experimental tests are commonly performed to predict the performance characteristics. Alternatively, CFD methods such as potential, viscous or hybrid methods can be a powerful tool for analysing the performance of podded propulsion systems.

Viscous solvers are capable of taking into account the effects of viscosity and turbulence due to the interaction between the propeller, pod and strut of a puller podded

propulsor at large azimuth angles. A RANS simulation for complete performance analysis of a podded propulsor was done by Sanchez-Caja et al. [16]. Ohashi and Hino [17] also studied this problem using a RANS solver with an unstructured mesh. Junglewitz and El Moctar [18] investigated the interaction between the podded propulsors' components in azimuthing condition. Liu et al. [14] used a propeller panel method code for predicting steady and unsteady forces, torques, and bending moments at various azimuth angles. Recently, Guo et al. [19], Amini et al. [15], Arikian et al. [20] and Shamsi and Ghassemi, [21] used unsteady RANS solver for simulating the flow around pulling and pushing podded propellers with azimuth angles. Achkinadze et al. [27] presented an improved velocity based source boundary element method as applied to modeling of podded propellers and propeller/rudder systems. Krasilnikov et al. [28] described some of the results with the numerical prediction of unsteady forces acting on propeller blades using a Reynolds Averaged Navier-Stokes (RANS) method. The paper presented recent validations results obtained with the method and illustrates the differences in forces experienced by a podded propeller operating in pulling and pushing modes at small azimuth angles.

The current paper presents the methodologies, result and discussions of a numerical simulation based research program to evaluate the effects of static azimuthing conditions on the propulsive characteristics of a podded propulsor in both puller and pusher configurations in open water. In a previous experimental campaign [3], the forces and moments in the three coordinate directions, the propeller shaft thrust and torque of a model pod at different static azimuthing conditions and propeller advance speeds for both puller and pusher configurations were measured. Physical phenomena and observations during the experiments are not described here in detail, but are presented in [3].

State of the art CFD capabilities have enabled the accurate prediction of forces and moments on the propeller as well as on the pod-strut body due to a small to moderate azimuthing angles. However, there is room for further improvement of the accuracy of the predictions at both heavy and light loading conditions. The primary aim of this research is to develop a simulation capability to capture most of the dynamics of podded propulsion systems in regular to extreme operating conditions. In the current research the commercial RANS Solver Star-CCM+ is extensively used for pod simulations and to investigate challenges in setting up effective podded propulsor simulations at azimuthing conditions for different pod configurations. Once confidence in CFD performance prediction of podded propulsors in such complex scenarios is developed, it is hoped that this tool will be a, less expensive alternative to experiments with propeller-pod-strut arrangements to obtain optimized size, shape and configurations of this prominent system.

2. PROPELLER AND POD MODELS

The numerical analyses included a model propeller with a pod consisting of a pod shell and a strut. A left-handed propeller with a hub taper angle of -15° was used in the puller pod and a right-handed propeller with a hub taper angle of 15° was used in the pusher pod. A description of the propeller characteristics is provided in Table 1. Further details of the geometry of the propellers are presented in [3].

Table 1: Geometric characteristics of the pusher and puller propellers used in the current study

Propeller Diameter	200 mm
No. of blade	4
Angular speed	15 rps
Sectional form	NACA 66 (DTMB Modified)
Section meanline	NACA = 0.8
planform shape	Blade planform shape was based on David Taylor Model Basin (DTMB) model P4119
EAR	0.60
Pitch distribution	Constant, P/D=1.0
Skew distribution	Zero
Rake distribution	Zero
Rotation	Left-handed (Puller); Right-handed (Pusher)

The geometrical particulars of the podded propulsor (pod-strut and the propeller) were selected to provide an average representation of in-service, full-scale single-screw podded propulsors. Figure 1 shows the rendered models of the bare propeller and the puller podded propulsor. The particulars of the pod-strut body tested are shown in Table 2. Further details of the geometry of the pod-strut are presented in [3].

Table 2: Propeller and pod dimensions used in the Numerical studies

External Dimensions of Model Pod	Values, Puller (mm)	Values, Pusher (mm)
Propeller Diameter	200.0	200.0
Hub Angle (degrees)	-15°	15°
Pod Diameter	102.96	102.96
Pod Length	303.7	303.7
Strut Height	222.22	222.22
Strut Distance	74.1	74.1
Strut Width	44.44	44.44
Strut Chord Length at Top	166.67	166.67
Strut Chord Length at Pod	232.0	232.0
Fore Taper Length	62.96	62.96
Aft Taper Length	81.48	81.48
Aft Taper Angle	-25°	25°
Fore Taper Angle	-15°	15°

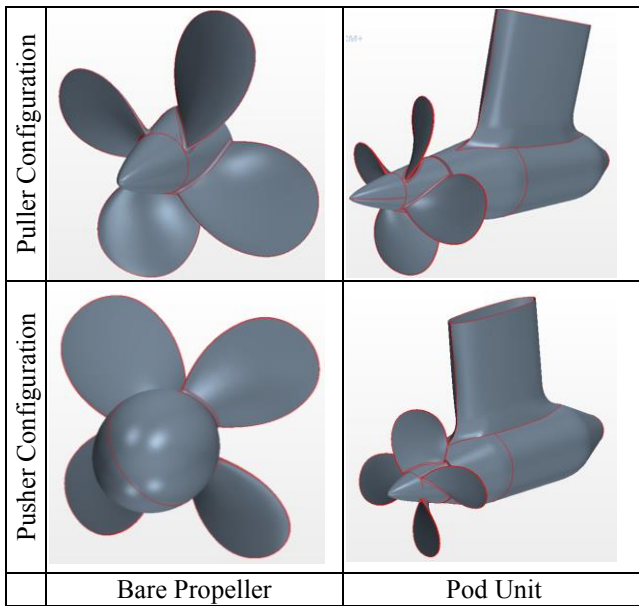


Figure 1: The bare propeller and the podded propulsor

3. SIMULATION METHODOLOGY

All computations reported here are performed using the CFD software Star-CCM+. This commercial RANS solver is based on a finite volume (FV) method and starts from conservation equations in integral form. With appropriate initial and boundary conditions and by means of a number of discrete approximations, an algebraic equation system solvable on a computer is obtained. First, the spatial solution domain is subdivided into a finite number of contiguous control volumes (CVs) which can be of an arbitrary polyhedral shape or structured cube shape and are typically made smaller in regions of rapid variation of flow variables. The time interval of interest is also subdivided into time steps of appropriate size (not necessarily constant). The governing equations contain surface and volume integrals, as well as time and space derivatives. These are then approximated for each CV and time level using suitable approximations.

3.1 GOVERNING EQUATIONS

The fluid is assumed to be incompressible. The governing equations are conservation of mass and momentum. Using the Reynolds averaging approach, the Navier-Stokes equations can be stated as:

$$\frac{\partial u_i}{\partial x_i} = 0 \quad (1)$$

$$\frac{\partial (\rho u_i)}{\partial t} + \frac{\partial}{\partial x_j} (\rho u_i u_j) = -\frac{\partial p}{\partial x_i} + \frac{\partial}{\partial x_j} \left(\mu \frac{\partial u_i}{\partial x_j} - \overline{\rho u_i' u_j'} \right) \quad (2)$$

where $-\overline{\rho u_i' u_j'}$ is the Reynolds stresses.

3.2 TURBULENCE MODEL

The standard two-equation $k-\omega$ turbulence model, which was popularized by Wilcox [24], incorporates modifications for low-Reynolds-number effects, compressibility, and shear flow spreading. This model is empirical, where one equation involves the turbulence kinetic energy (k) representing the velocity scale, and the other takes the turbulent dissipation rate (ω) into account representing the length scale. The standard two-equation $k-\omega$ model turbulence model accounting for the effect on turbulence is:

$$\frac{\partial}{\partial t} (\rho k) + \frac{\partial}{\partial x_i} (\rho k u_i) = P_k - \rho \beta^* k \omega + \frac{\partial}{\partial x_i} \left[\left(\mu + \frac{\mu_t}{\sigma_k} \right) \frac{\partial \omega}{\partial x_j} \right] \quad (3)$$

$$\frac{\partial}{\partial t} (\rho \omega) + \frac{\partial}{\partial x_i} (\rho \omega u_i) = \alpha \frac{\omega}{k} P_k - \rho \beta \omega^2 + \frac{\partial}{\partial x_i} \left[\left(\mu + \frac{\mu_t}{\sigma_\omega} \right) \frac{\partial \omega}{\partial x_j} \right] \quad (4)$$

where σ_k and σ_ω are the turbulent Prandtl numbers for k and ω , respectively, and

$$P_k \approx \mu_t \left(\frac{\partial u_i}{\partial x_j} + \frac{\partial u_j}{\partial x_i} \right) \frac{\partial u_i}{\partial x_j}$$

is the rate of production of turbulent kinetic energy. The turbulent viscosity, μ_t , is computed by combining k and ω as follows:

$$\mu_t = \alpha^* \rho \frac{k}{\omega} \quad (5)$$

The coefficient α^* damps the turbulent viscosity causing a low-Reynolds-number correction [26].

3.3 PROPELLER SIMULATION METHOD

The rotation of the propeller is modeled using two approaches: steady and unsteady. For the steady state case, the rotation of the propeller in the fluid environment is modelled in a steady-state manner by using the Moving Reference Frame (MRF) method in RANS solver. A rotating reference frame is a rotating frame of reference that can be applied to regions to generate a constant grid flux. This approach gives a solution that represents the time-averaged behavior of the flow, rather than the time-accurate behavior.

In the steady case, the governing equations are solved with additional acceleration terms. The computational domain is divided into stationary and moving frames. For

an arbitrary point in solution field, the absolute velocity, \vec{v} and relative \vec{v}_r can be defined by the following relation:

$$\vec{v}_r = \vec{v} - (\vec{\Omega} \times \vec{r}) \quad (6)$$

where \vec{r} is the position vector from the origin of the moving frame and $\vec{\Omega}$ is the angular velocity vector.

The governing equations of fluid flow in a moving reference frame can be written in two different ways: absolute velocity formulation or relative velocity formulation. The mass and momentum equation in the relative velocity formulation can be stated as:

$$\frac{\partial \rho}{\partial t} + \nabla \cdot (\rho \vec{v}_r) = 0 \quad (7)$$

$$\frac{\partial}{\partial t} (\rho \vec{v}_r) + \nabla \cdot (\rho \vec{v}_r \vec{v}_r) + \rho (2\vec{\Omega} \times \vec{v}_r + \vec{\Omega} \times \vec{\Omega} \times \vec{r}) = -\nabla p + \nabla \cdot (\vec{\tau}) \quad (8)$$

where $\rho (2\vec{\Omega} \times \vec{v}_r)$ is the Coriolis acceleration and $(\vec{\Omega} \times \vec{\Omega} \times \vec{r})$ is the centripetal acceleration.

In the unsteady approach, the sliding mesh technique was used to simulate the time-accurate behavior of the propeller. In this approach, the mesh vertices of a propeller region move at the required rotational speed during a transient analysis. This mesh motion is specified using either a rotation motion or a rotation and translation motion. For highly unsteady conditions, the sliding mesh approach is expected to give better results. Both the moving reference frame and unsteady sliding mesh approaches to propeller modeling require creating a separate region for the moving propeller blades. The interface between the stationary and rotating regions are defined to provide special attention during the meshing process. Conformal meshes are preferred for the regions with the interface.

3.4 NUMERICAL MESH AND BOUNDARY CONDITIONS

The numerical method discussed above is employed for the simulation of viscous flow around a bare propeller and a podded propulsor in the two configurations. The fluid domain around the propeller is considered using rotating and fixed cylindrical frames. The rotating frame simulates the propeller rotation and employs the Coriolis acceleration terms in the governing equations for the fluid. In the bare propeller case, the fixed frame is a circular cylinder with $5D$ diameter, where D is the propeller diameter. The distance between the rotating frame and inlet is nearly $4D$, while it is nearly $6D$ for the outlet and dynamic frame. The simulation domain for the pod was a rectangular cube. The positions of inlet and

outlet are respectively $3L_{Pod}$ and $5L_{Pod}$, where L_{Pod} is the pod length. The positions of the sides and bottom are respectively $4L_{Pod}$ and $4L_{Pod}$, respectively. This setup was used for pod in straight-ahead condition. For the pod at azimuthing angles, the domain was extended on one of its sides depending on the azimuthing angle.

Figure 2 show the 3D computational domain for single propeller and a podded propulsor. For both bare propeller and pod propulsor cases, the solution field is divided into four blocks with each block meshed with unstructured polyhedral cells. The use of the unstructured grid results in a smoother discretization near the leading and trailing edge of the propeller. Figure 3 shows the volume mesh for the bare propeller and the podded propulsor on a vertical plane through the propeller center. It also shows the volume mesh for the podded propulsor at 30° azimuthing condition on a horizontal plane through the propeller center.

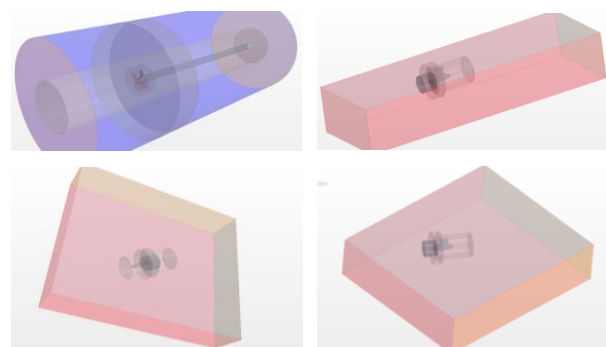


Figure 2: The Mesh block of simulation field: clockwise from top-left: podded propeller, puller pod at 0° , pod with positive azimuthing angle, and pod at negative azimuthing angle

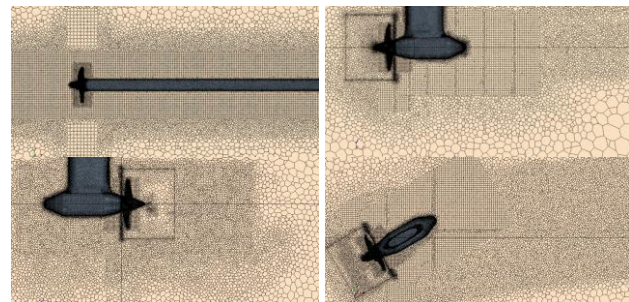


Figure 3: The vertical plane showing the volume mesh around, from top-left clockwise: the bare propeller, the puller podded propulsor, the pusher podded propulsor, and the puller podded propulsor at 30° azimuthing condition.

In order to properly account for viscous effects and complex flow patterns, it is necessary to employ accurate and robust numerical methods which can provide detailed resolution of the propeller boundary layer, turbulent wake, leading edge separation, and unsteady ring vortices induced by the propeller operating in front of a pod-strut body with large azimuth angles. Extreme

care was taken to arrange the meshing around the propeller blades. Figure 4 presents a close-up view of the meshing arrangement around the propeller blades and the pod-strut body. It was challenging to set up the meshing as the pod-strut was stationary whereas the propeller was revolving. Local refinements were applied around the leading and trailing edges of the propeller blades. Additionally, a total of 6 prism layers were applied to the propeller blades and pod-strut body to make sure the strong viscous effect is captured accurately near the boundary of the propeller blades and the pod.

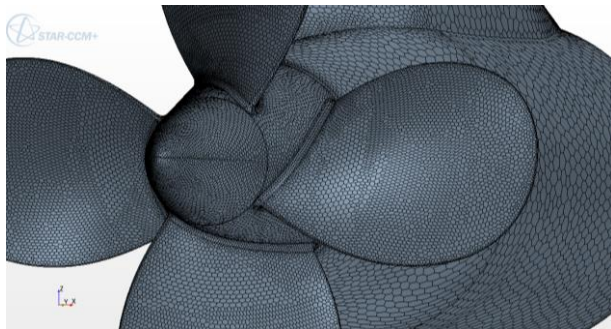


Figure 4: The close up view showing the Meshing Arrangement around the propeller Blades and the pod-strut body.

The inlet boundary condition for the fixed frame is set as a velocity inlet with a constant velocity profile. The outlet boundary condition can be set as a pressure outlet for this frame. Thus the free surface was not modelled, a free slip wall was assumed instead. This is similar to the experiment condition, where the free surface was suppressed using a round boat right above the strut [3]. The propeller blades, pod, strut, and the fixed cylinder are assumed as no-slip wall boundary conditions.

Both mesh and time step sensitivity studies were carried out to find the best compromise between mesh size, computational time and prediction accuracy. The simulation conditions examined in the study are presented in Table 3. The total number of mesh and the total simulation time are provided in the table. Note that there was a significant increase of simulation time when unsteady setup was used.

The propeller-pod-strut geometry was modelled in the RANS solver by setting up the geometry, generating surface mesh, boundaries, volume mesh, solver and physics. The governing equations are solved by the finite volume method based on the RANS equations. The SIMPLE algorithm is used to solve the pressure-velocity coupling equations. The second order upwind discretization scheme is utilized for the momentum, turbulent kinetic energy, and turbulent dissipation rate. The simulations are completed both in steady state using the MRF and in unsteady state using the SM techniques for $\pm 30^\circ$ azimuthing angle for both pod configurations. The turbulence is modelled by Menter's SST $k-\omega$ method [25]. Note that unsteady state simulations are generally

more applicable where flow swirl and extreme separation are expected.

Table 3: Simulation Conditions Examined in the Study

Case	Pod-Strut	Solution Type	Azimuth Angle	Adv. Coeff.	Total Mesh(M)	Time (hrs)
1	Puller and Pusher Propeller			0.2, 0.5, 0.8	1.65	3
2	Puller	Steady	0	0.0, 0.2, 0.5, 0.8, 1.0	1.82	5
3	Pusher	Steady	0	0.0, 0.2, 0.5, 0.8, 1.0	2.05	5.5
2	Puller	Steady	$0, \pm 15, \pm 30$	0.2, 0.5, 0.8	2.75	7
3	Pusher	Steady	$0, \pm 15, \pm 30$	0.2, 0.5, 0.8	2.95	8
4	Puller	Unsteady	$0, \pm 30$	0.2, 0.5, 0.8	3.65	42
5	Pusher	Unsteady	$0, \pm 30$	0.2, 0.5, 0.8	3.75	45

Segregated flow simulation conditions were used for both steady case and unsteady cases. Simulations were run sufficiently long to obtain convergence; generally 3000 iterations for steady state were sufficient and 25000 iterations for unsteady state simulations. In the unsteady simulations, different time step in the range of 0.0001s to 0.001111s was examined. The time step size is chosen such that one propeller revolution is computed in 60 time steps, or equivalently $\Delta t = 0.001111$. It was found that a time step of smaller than 0.001111s does not significantly improve the simulation results but considerably increase the simulation time. For all unsteady simulations a time step of 0.001111s was used.

The number of inner iterations per time steps was varied between 5 to 25 and 15 seemed high enough to obtain convergence. This means approximately 25000 interactions or 2 seconds (30 propeller revolutions) of simulation time was required in order to obtain convergence in the unsteady state simulations. An asymptotic condition was also established to optimize the inner iteration number for the simulations with the pod at 30° azimuthing condition and was found to be time saving.

3.5 ADAPTIVE MESHING TECHNIQUE

The flow conditions around the propeller and pod body is expected to be very complex, especially at higher

azimuthing angle. Complex interactions between the uniform inflow, propeller wake and pod-strut wake are expected to occur and this requires further refinement of critical zones. It was unknown from the outset where and how to refine the critical areas. In the current simulations automatic refinement of meshing arrangement, based on flow conditions, was established to ensure the complex flow interactions are captured. Conditions were set based on the velocity magnitude difference between adjacent cells within the domain to refine the respective cells. A total of three mesh refinement conditions were set to refine the mesh. The refined mesh for all azimuthing angles along with the velocity magnitude difference are shown in Figure 5, which demonstrated the velocity distribution and its influence on the meshing distribution in the entire domain.

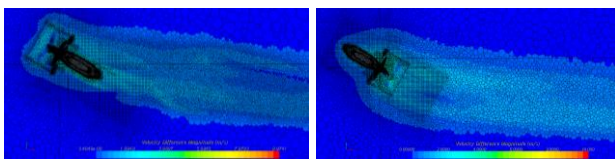


Figure 5: Refined Meshing for Puller (left) and pusher (right) Pods Arrangement using Automated Mesh Table at -30° and +30° Azimuth Angle

4. RESULTS AND DISCUSSIONS

This section presents a detailed discussion of the trend of the coefficients of the propeller and the pod unit with the change of the propeller loading (inflow velocity) and azimuthing angle in static azimuthing conditions as obtained from the respective simulations. A discussion on the coordinate system used to interpret the results is presented. The results of the mesh and time step sensitivity studies are also presented in this section. The predicted results are compared with the corresponding measurements obtain in [3 and 12]. Discussions on the pressure and velocity distribution on and around the propeller-pod-strut bodies obtained from the simulations are presented

A detailed discussion on the validity and uncertainty of the measurements is provided in [3 and 12]. Note, both the experiment and numerical simulations are carried out in the same scale. It is possible to encounter potential correlation issue between the experimental data and corresponding numerical simulation results due to the scale effect, turbulence states etc., especially at high azimuthing angle of greater than 30°, when separation of flow may arise. The separation location on the propeller and pod-strut surfaces, vortex shedding and overall turbulence states of the flow around the propeller-pod-strut bodies may be different in the experimental and numerical simulation conditions and these may significantly affect the end results. However, the authors believe for azimuthing angle lower than 30° may not have the flow separation issue, thus the scale effect could be minimal. Further investigation is required to better understand this issue, by carrying out full scale simulations and comparing the flow fields at various scales.

4.1 COORDINATE SYSTEM

The definition of the forces, moments and co-ordinates that was used to analyze the data and present the results is shown in Figure 6. A right handed coordinate system with positive Z downward is used for the carriage fixed system. The coordinate centre was situated 0.5m vertically above the pod centre, which is at the intersection of the horizontal axis through the propeller shaft centre and the vertical axis through the strut shaft centre. The propeller thrust and torque were measured at the propeller end of the shaft. The propeller forces, pod forces and moments are presented in the form of traditional non-dimensional coefficients as defined in Table 4.

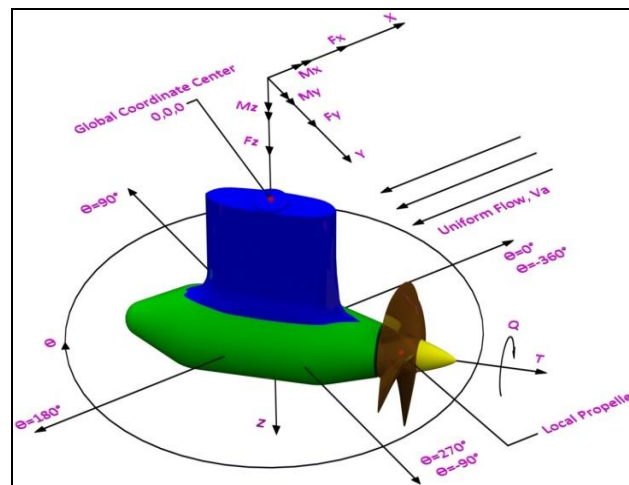


Figure 6 – Definitions of forces, moments, coordinates of the puller azimuthing podded propulsors.

Table 4 – Data reduction equations and definitions of parameters used to present the experimental data.

Performance Characteristics	Data Reduction Equation
K_T – propeller thrust coefficient	$T / \rho n^2 D^4$
K_{FX} – axial force coefficient,	$F_X / \rho n^2 D^4$
$10K_Q$ – propeller torque coefficient	$10Q / \rho n^2 D^5$
J – propeller advance coefficient	V_A / nD
η_{prop} – propeller efficiency	$J / 2\pi \times (K_T / K_Q)$
η_{pod} – pod efficiency	$J / 2\pi \times (K_{FX} / K_Q)$
K_{FY} – side force coefficient	$F_Y / \rho n^2 D^4$
K_{FZ} – vertical force coefficient	$F_Z / \rho n^2 D^4$
K_{MX} – moment coefficient around x axis	$M_X / \rho n^2 D^5$
K_{MY} – moment coefficient around y axis	$M_Y / \rho n^2 D^5$
K_{MZ} – moment coefficient around z axis (steering moment)	$M_Z / \rho n^2 D^5$

where, T - propeller thrust; Q - propeller torque; ρ - water density; n - propeller rotational speed; D - propeller diameter; V_A - propeller advance speed, in the direction of carriage motion

$F_{X, Y, Z}$ - components of the hydrodynamic force on the pod

$M_{X, Y, Z}$ - components of the hydrodynamic moment on the pod

4.2 MESH SENSITIVITY STUDY

A mesh convergence and validation study was performed using the puller podded propulsor with a moderately loaded propeller (advance coefficient of 0.50). In this study, the same domain blocks were used as in Figure 2, but different element sizes were considered. The best compromise between element size and accuracy has been obtained from the results of this work. Ten models in the same domain with different element sizes and cell numbers were generated, see Table 5. These models were simulated at an advance coefficient of 0.5 (inflow speed of 1.5 m/s), shaft rotational speed of 15 rps and at 0° pod angle of attack. The simulation results were compared to the data acquired during the experimental program, see Figure 7. The variation of error values for the propeller thrust and torque and pod F_X are shown in Table 5. The errors were reduced as the number of elements increased.

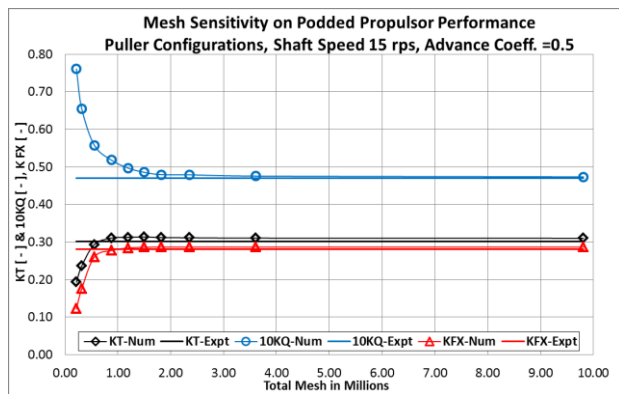


Figure 7 – Mesh Convergence Study Results for Propeller Thrust and Torque and Pod F_X for the Puller Podded Propulsor at Advance Coefficient of 0.5.

Note that no mesh sensitivity study was carried out for the puller or pusher propulsor in oblique flow conditions. However, the above sensitivity study provided guidelines to select the mesh base size for all configurations. The remaining simulations with pod-strut-propeller assembly were carried out with the base mesh size on the puller propulsor. This gives a total mesh of 1.8 M; See case 4 in Table 5. The gain in the accuracy of the simulations with any further increase in the mesh size may be considered insignificant. Additionally, the adaptive meshing feature available in the code was also used, especially for the high azimuthing cases ($\pm 30^\circ$), see section 3.5.

Table 5 – Summary of Results from Mesh Convergence Study

Case	Mesh Parameters			% Diff Simulation and Targets		
	% Base Size	Base Size (m)	No of Cells (M)	Thrust T	Torque Q	Pod FX
1	50%	0.05	9.81	-2.96%	-1.18%	-1.68%
2	75%	0.075	3.60	-3.10%	-1.85%	-1.68%
3	90%	0.09	2.36	-3.43%	-2.98%	-1.68%
4	100%	0.10	1.82	-3.63%	-3.18%	-1.68%
5	110%	0.11	1.50	-4.15%	-5.16%	-1.52%
6	125%	0.125	1.20	-3.83%	-8.90%	-0.90%
7	150%	0.150	0.88	-3.18%	-15.98%	1.29%
9	200%	0.2	0.55	2.55%	-29.13%	7.08%
9	300%	0.3	0.31	21.54%	-61.53%	35.26%
10	400%	0.4	0.22	35.77%	-96.56%	52.65%

4.3 STEADY AND UNSTEADY SIMULATIONS

Both time-averaged steady state and time accurate unsteady state simulations were completed for the pod in straight-ahead and $\pm 30^\circ$ azimuthing angles; see Figure 8.

It is illustrated in the figures that that the difference in propeller thrust and torque as well as the loads on the pod-strut body between the steady and unsteady state simulations were minimum for pod in straight-ahead condition. However, at the high azimuthing angle of $\pm 30^\circ$, the differences were significant and the results from the unsteady simulations were used to compare that of the corresponding measurements; See Figure 8. The propeller thrust and torque for $\pm 30^\circ$ azimuthing angles were significantly different and closer to the measurements when unsteady simulations were used. A similar observation was made for both puller and pusher pods. Note in Table 3 that performing the simulations in unsteady state setup takes approximately three times longer than in steady state setup for a similar simulation. Considering the improvement in accuracy of the predictions, it may be logical to use the unsteady state setup for simulations to predict performance of pod unit in the advanced design stages; steady state simulations may be accurate enough in early design stages.

The steady state solution represents an instantaneous quasi-steady solution in which the upstream effects from the pod induces a non-uniform effective wake to the propeller, which is not captured. The steady assumption may also be flawed due to the transient flow around the pod-strut at high azimuthing angles. The unsteady time-accurate solution is expected to capture the non-uniform inflow to the propeller and the separation on the pod-strut body. The comparison above shows that the high separation, propeller swirl and the interaction between the propeller wash and pod-strut body was captured more accurately in the unsteady state simulations. However, the unsteady simulations took significantly longer time to converge as compared to the steady ones, hence were only used where appropriate.

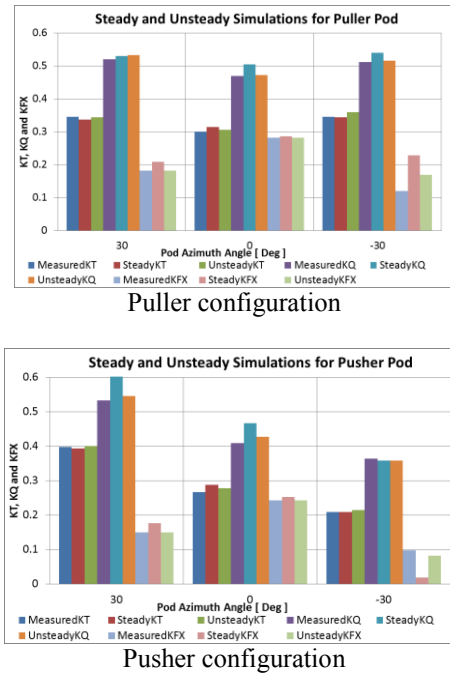


Figure 8 – Comparison of propeller and pod performance parameters for the puller and pusher pods at multiple azimuthing angles at advance coefficient of 0.5, obtained from steady and unsteady simulations

4.4 BARE PROPELLER PERFORMANCE

The measurements and predictions of the open water characteristics of the bare puller and pusher propellers are presented in Table 6 and in Figure 9 and Figure 10, which show a good agreement between the approaches. The predicted thrust and torque were within 2% and 4% of the measurements, respectively. For both propeller cases, the thrust is slightly under predicted, while the torque is over predicted. In the RANS simulation the flow is assumed to be fully turbulent whereas the model experiments primarily occur in transient flow conditions. This may causes higher skin friction on the blades in the prediction compared to the measurements.

Table 6: Comparison of Thrust and Torque between Measurements and Predictions in the Propeller Only Case

	J	Measurement		Prediction		% Difference	
		KT	10KQ	KT	10KQ	KT	10KQ
Puller	0.20	0.4128	0.6025	0.4083	0.6139	1.1%	-1.9%
	0.50	0.2853	0.4407	0.2833	0.4611	0.5%	-3.4%
	0.80	0.1340	0.2640	0.1417	0.2875	-1.8%	-3.9%
Pusher	0.20	0.3923	0.5794	0.3941	0.5960	-0.5%	-2.9%
	0.50	0.2636	0.4221	0.2735	0.4209	-2.5%	0.2%
	0.80	0.1326	0.2563	0.1368	0.2617	-1.1%	-0.9%

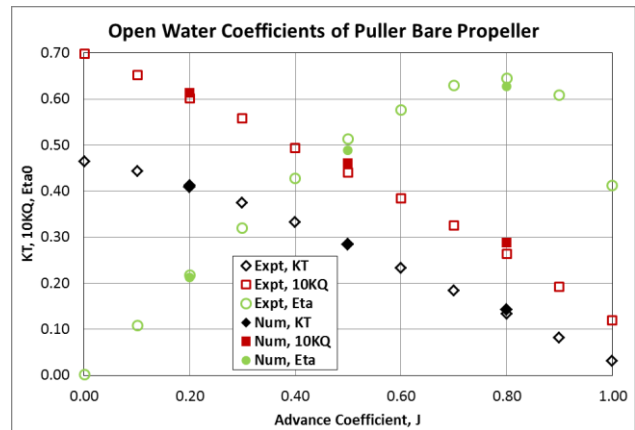


Figure 9: Open water characteristics of bare propeller in puller configuration

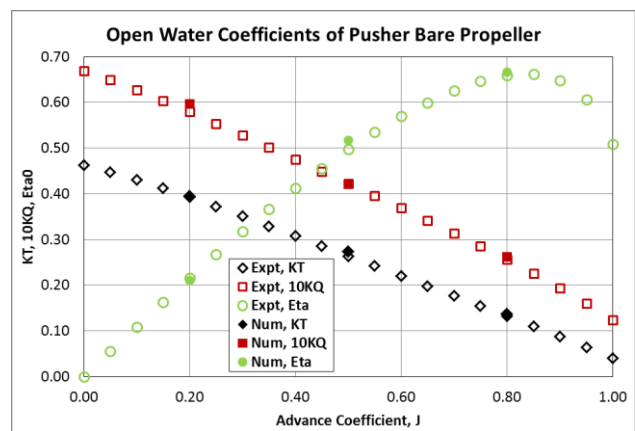


Figure 10: Open water characteristics of bare propeller in pusher configuration

Note, % difference values in Table 6 and other similar tables in this paper are calculated using the following formulation:

$$\%q = \frac{Q_{P1} - Q_{P2}}{Q_{P1|J-Lowest}} \times 100 \quad (9)$$

where, Q is the performance parameter under consideration, subscripts $P1$ and $P2$ represent measured and predicted values, respectively, $J-Lowest$ means the value of the parameter at the lowest advance coefficient. Symbol $\%q$ stands for the difference between the measured and predicted values as a percentage of the measured ones.

Figure 11 presents the pressure and velocity distribution on back side and face side of the propeller for the puller and pusher propellers. As observed in the figure, high pressure is on the face and low pressure is on the back side. The minimum pressures are located on the leading edge of the propeller blades, close to the tip. The figure also shows the velocity vector at the propeller tips to demonstrate the tip vortices.

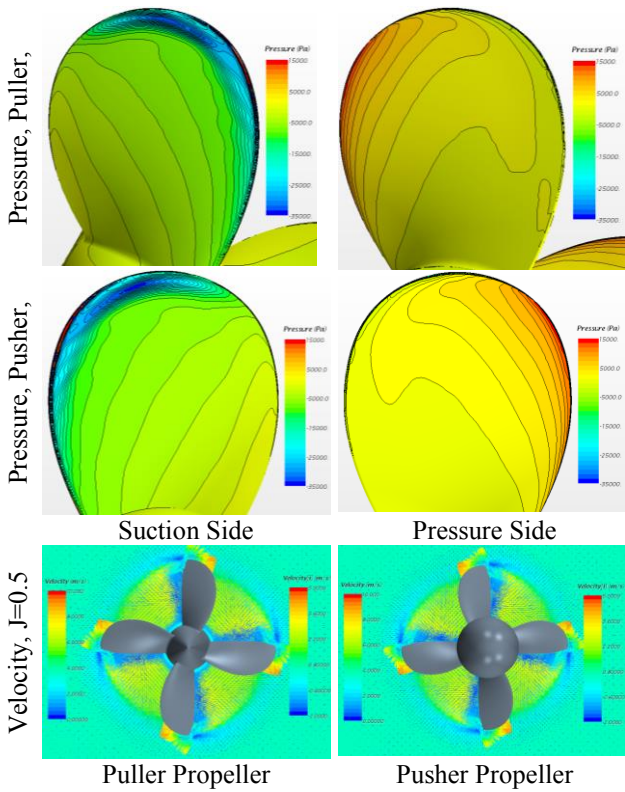


Figure 11: The pressure and Velocity (vector) distribution on the bare puller propeller.

4.5 PODDED PROPULSORS IN STRAIGHT-AHEAD CONDITION

The comparison of measured and predicted propulsive performance of the puller and pusher pod units in straight ahead condition for different propeller loading conditions are provided in Table 7 as well as in Figure 12 and in Figure 13. Note, using steady state simulations, the accuracy of K_T , K_Q and KF_X were primarily within 6% for all loading conditions and pod configurations.

Table 7: Comparison of Propeller Thrust and Torque and Unit Thrust between Measurements and Predictions for Puller and Pusher Pod Units in Straight Ahead Condition

		Measurements			Predictions			% Difference		
		KT	10KQ	KFX	KT	10KQ	KFX	KT	10KQ	KFX
Puller	0	0.492	0.668	0.484	0.501	0.702	0.462	-1.7	-5.1	4.5
	0.2	0.425	0.602	0.409	0.439	0.622	0.413	-2.9	-2.9	-0.8
	0.5	0.301	0.470	0.282	0.314	0.480	0.287	-2.7	-1.4	-1.0
	0.8	0.158	0.293	0.135	0.177	0.320	0.145	-3.8	-3.9	-2.2
	1	0.070	0.170	0.027	0.086	0.198	0.047	-3.1	-4.1	-4.0
Pusher	0	0.461	0.651	0.452	0.460	0.674	0.429	0.2	-3.4	5.0
	0.2	0.394	0.568	0.378	0.407	0.587	0.373	-2.8	-2.9	1.1
	0.5	0.266	0.410	0.243	0.290	0.448	0.255	-5.1	-5.8	-2.6
	0.8	0.151	0.267	0.108	0.167	0.301	0.131	-3.4	-5.1	-5.0
	1	0.066	0.154	0.019	0.079	0.183	0.030	-2.8	-4.5	-2.4

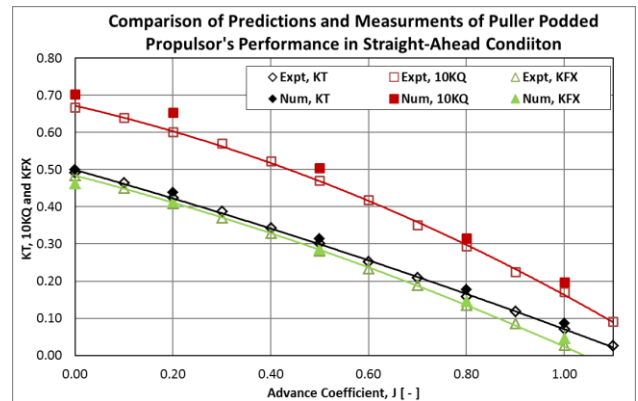


Figure 12: Validation of Numerical Simulation of Puller Pod Performance Characteristics at Straight-Ahead Condition

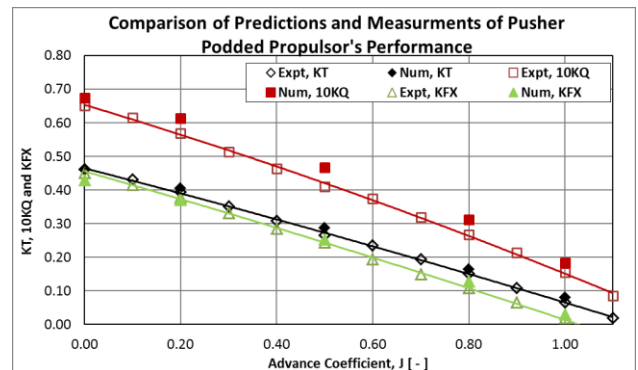


Figure 13: Validation of Numerical Simulation of Pusher Pod Performance Characteristics at Straight-Ahead Condition

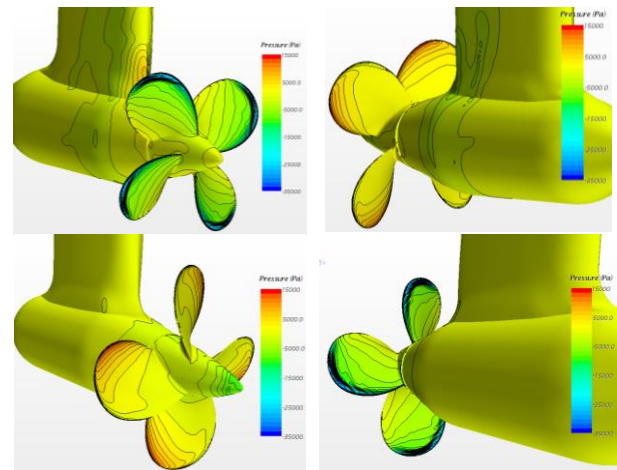


Figure 14: Surface Pressure Contour (Left and Right Sides, Looking Towards Downstream) of Podded Propulsor at $J=0.2$; Top-Puller Configuration, Bottom-Pusher Configuration

The velocity and pressure distributions on the propeller faces and on the pod body surface for the two configurations are provided in Figure 14. The velocity and pressure distributions in the propeller plane for the puller and pusher propellers at multiple loading conditions are presented in Figure 15 and Figure 16, respectively. For the puller configuration, the strut and pod are located downstream of the propeller, so the induced velocities from the propeller influence the inflow to the strut and pod. Therefore, the surface pressure contours of

the pod and strut are asymmetrical, see top of Figure 14. In the pusher configuration, the propeller works in the wake of the strut. Cross flows from the pod and strut have tangential and radial velocity. This leads to a strongly non-uniform inflow for the propeller but minimal influence on the pod-strut body.

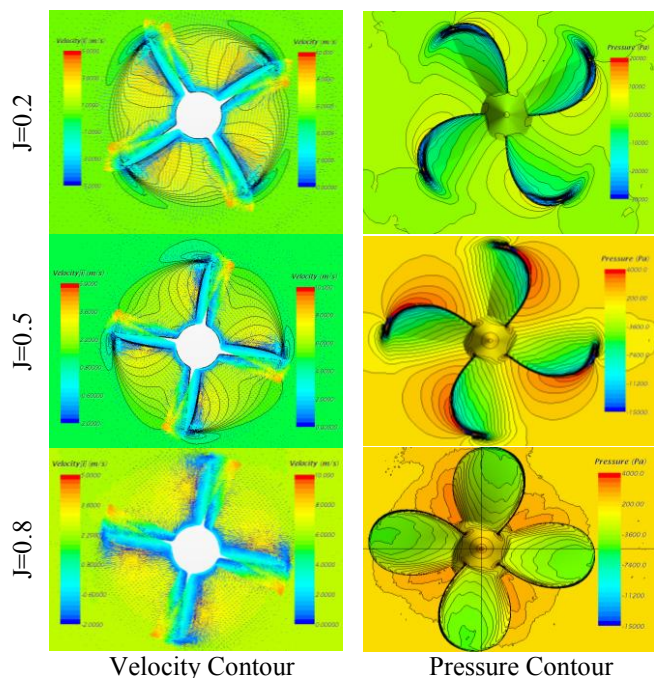


Figure 15: Velocity and Pressure Contours at the Propeller Centre Plane of Puller Unit in Straight-ahead Condition at Various Loading Conditions

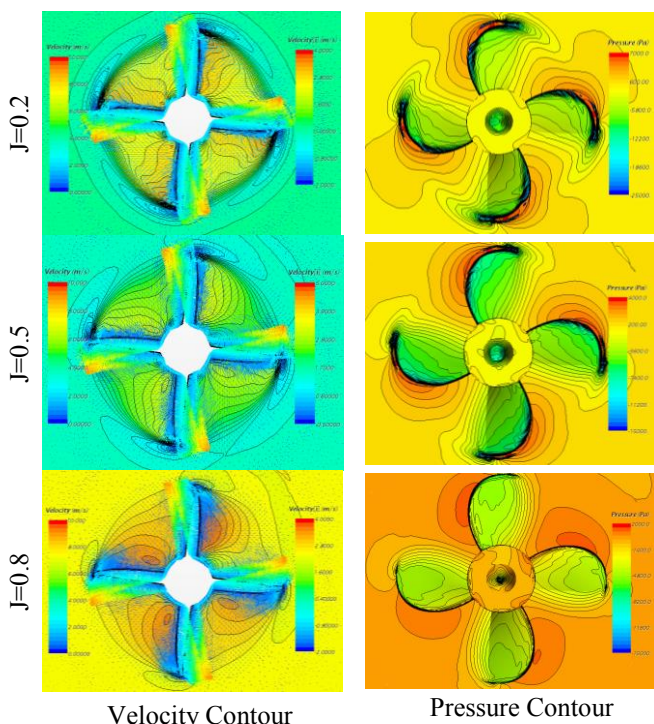


Figure 16: Velocity and Pressure Contours at the Propeller Centre Plane of Pusher Unit in Straight-ahead Condition at Various Loading Conditions

4.5 PODDED PROPULSORS IN AZIMUTHING CONDITION

The propulsive performance of the puller and pusher podded propulsors are studied in azimuthing conditions and the results are compared with the corresponding experimental data. The results included are the propeller thrust coefficient, propeller torque coefficient, pod unit axial force coefficient, pod unit side force coefficient and pod unit steering moment coefficient at various azimuthing angles and propeller loading conditions.

The propeller thrust and torque coefficients for the puller and pusher propulsor in multiple static azimuthing angles from 0° to $\pm 30^\circ$ are presented in Figure 17 through Figure 20. Note, the predicted results from both the steady state and unsteady state simulation conditions are presented in the figures. A second order curve is fit through the measured data. Table 8 and Table 9 present the percentage difference of the pod performance coefficients between the measurements and predictions at multiple loading conditions, azimuthing angles and pod configurations. It is noted that the curves of the propeller thrust coefficients are symmetrical at positive and negative azimuthing angles, which are well captured in both steady and unsteady simulations. The same behavior is found in the propeller torque coefficient. In azimuthing condition, the effective advance velocity ratio in the direction of the propeller axis is reduced; this results in a higher thrust in the azimuthing cases as compared to straight-ahead case.

For the puller configuration, there is a reasonably good agreement between the steady state simulation and the experimental results when the azimuthing angle was between 0 to $\pm 30^\circ$. The relative errors of K_T and K_Q are less than 12% and 15% when steady state setup was used. This difference may be attributed to the flow separation and strong propeller-pod-strut interaction, which may not be well captured in the steady state solution. A significant improvement in predicting the thrust and torque was noticed in the results of the unsteady state simulations, especially for the $\pm 30^\circ$ azimuthing conditions. The maximum error in K_T was reduced to approximately 6% and K_Q to 8% at the lightly loaded condition.

In pusher configuration, for all advance coefficient values, the propeller thrust coefficient increases when azimuthing angle is increased from negative angles to positive angles and the propeller thrust coefficients is not symmetrical at positive and negative azimuthing angles. The same trend can be seen for the torque coefficient. In pusher configuration, propeller works in the wake of strut, the inflow on the propeller is strongly non-uniform. Due to differences in the inflow condition for positive and negative azimuthing angle, asymmetry is seen in the propeller thrust and torque curves. The RANS simulations captured this trend well with both steady and unsteady setup provided close comparison with the

measurements. The prediction accuracy improved considerably when unsteady state simulations were used, especially for $\pm 30^\circ$ azimuthing angle cases, see Table 9.

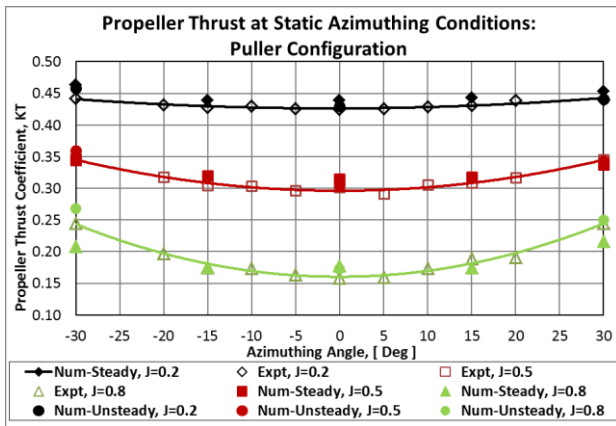


Figure 17 – Comparison of experimental and numerical results of propeller thrust coefficient of the puller pod.

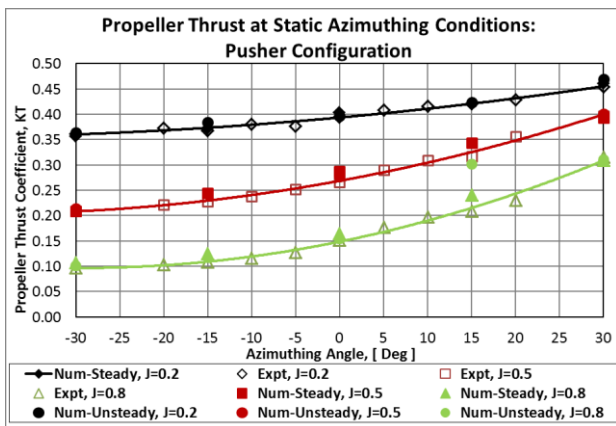


Figure 18 – Comparison of experimental and numerical results of propeller thrust coefficient of the pusher pod.

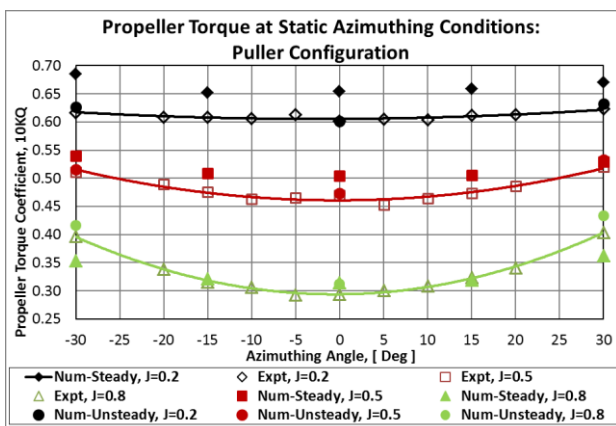


Figure 19 – Comparison of experimental and numerical results of propeller torque coefficient of the puller pod

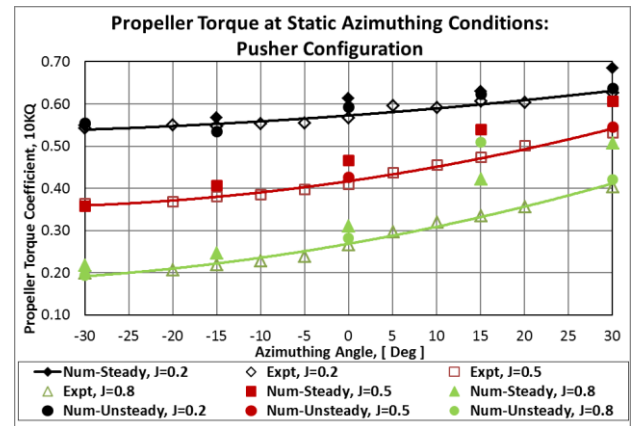


Figure 20 – Comparison of experimental and numerical results of propeller thrust coefficient of the pusher pod

Both the measurements and the RANS predictions showed that the axial force coefficient, KF_x , as shown in Figure 21 and Figure 22, decreased for both azimuthing directions but the reduction was visibly stronger for negative azimuthing angles. The side force coefficient, as shown in Figure 23 and Figure 24, showed strong dependency on azimuthing angle. The side force coefficients increased with both positive and negative azimuthing angles from the straight-ahead position. Due to the propeller wake rotation and strut interactions, there is a small side force in straight-ahead condition for both puller and pusher configurations, more visible for puller case. A similar trend is seen for the steering moments for the puller and pusher configurations, respectively, see Figure 25 and Figure 26.

Good agreement between the predictions and measurements for pod unit force, side force and steering moment was achieved for all azimuthing angles and loading conditions. The differences in the pod global forces and steering moment between the steady and unsteady simulation cases as compared to the measurements were small. The primary cause of this discrepancy is the viscous effects and the interaction between the propeller, pod and strut. Due to viscous effects at the high azimuthing angle of $\pm 30^\circ$, the interaction become dominant and the drag forces of the propeller, pod and strut increases because of flow separation. The steady-state calculations with the MRF method does not model the unsteadiness of the flow separation, hence is not sufficient enough to capture these effects. Generally the unsteady state simulations predicted the forces more accurately than the steady state simulations, especially for $\pm 30^\circ$ cases.

The side force and steering moment coefficients change approximately linearly with the change of azimuthing angle in the moderate range of azimuthing angles of $\pm 30^\circ$. It is observed that the shaft thrust and torque as well as axial force were steady when the azimuthing angles were within $\pm 30^\circ$. The predicted results acquired by the time accurate simulations captured these phenomena more accurately than the steady state ones.

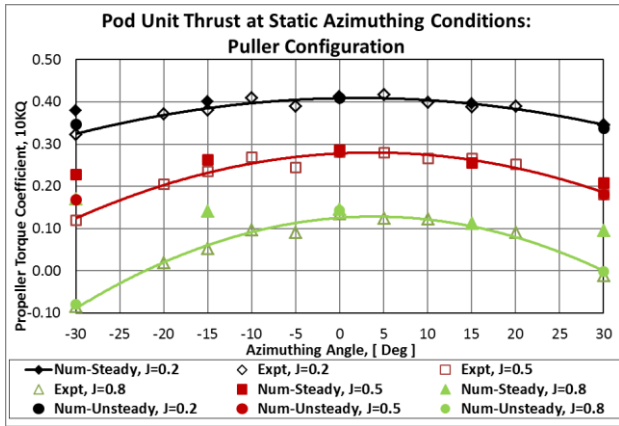


Figure 21 – Comparison of experimental and numerical results of axial force coefficient of the puller pod.

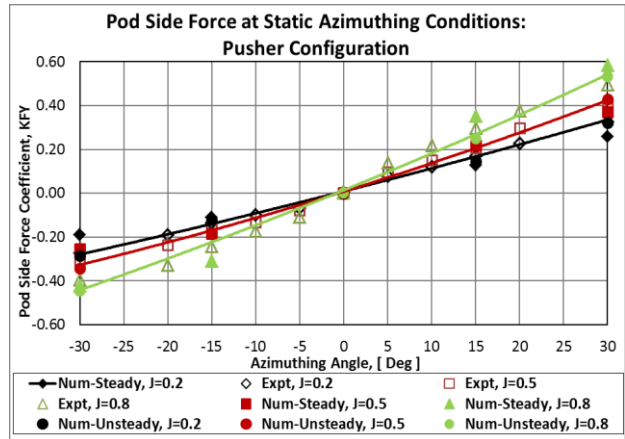


Figure 24 – Comparison of experimental and numerical results of side force coefficient of the pusher pod.

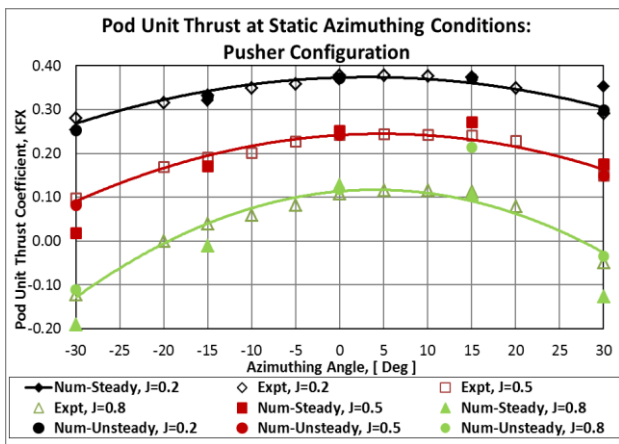


Figure 22 – Comparison of experimental and numerical results of axial force coefficient of the pusher pod.

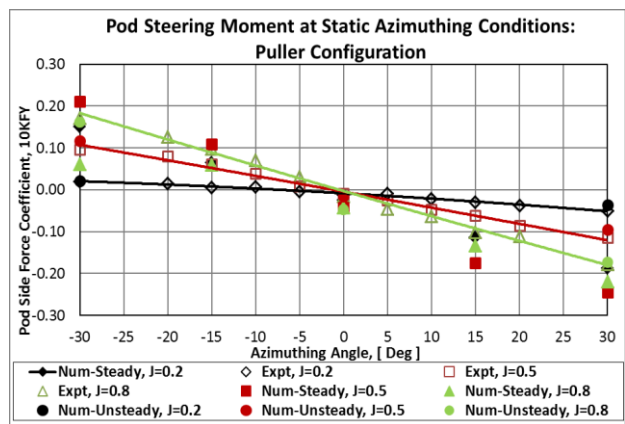


Figure 25 – Comparison of experimental and numerical results of steering moment coefficient of the puller pod.

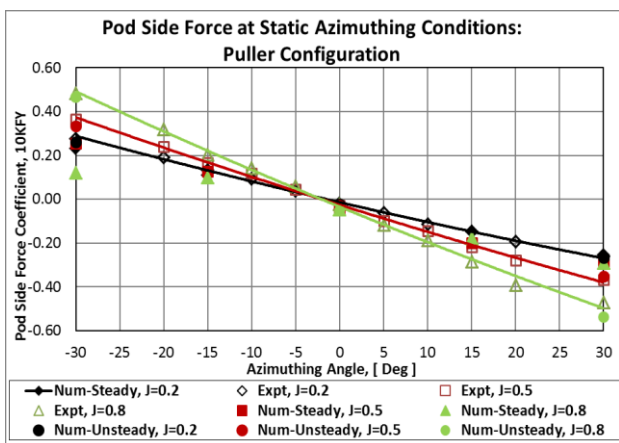


Figure 23 – Comparison of experimental and numerical results of side force coefficient of the puller pod.

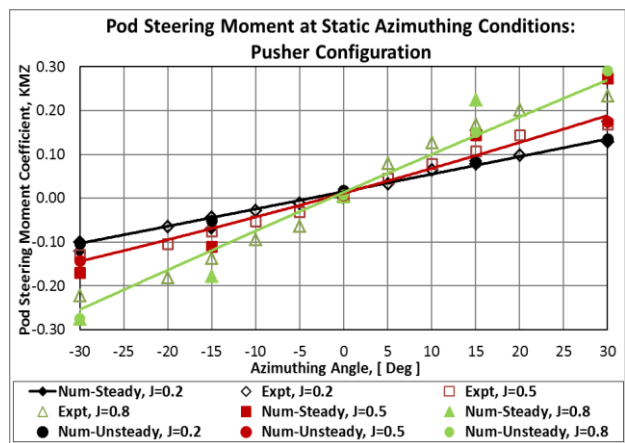


Figure 26 – Comparison of experimental and numerical results of steering moment coefficient of the pusher pod.

Table 8: Percentage difference between Measurements and Predictions of pod performance coefficients using steady and unsteady simulation conditions for puller Pod in difference azimuthing conditions.

		Steady			Unsteady		
		30	0	-30	30	0	-30
J=0.2	KT	11.90%	-3.40%	-4.80%	-0.30%	-1.20%	-3.80%
	KQ	8.40%	-8.70%	-11.10%	-1.60%	0.00%	-1.60%
	KFX	1.20%	-1.00%	-17.80%	1.90%	-0.20%	-8.00%
	KFY	4.90%	14.30%	16.40%	-2.40%	-8.10%	6.20%
	KMZ	63.20%	109.20%	684.00%	26.70%	-8.40%	-9.00%
J=0.5	KT	2.30%	-4.40%	0.60%	0.30%	-1.70%	-3.80%
	KQ	-1.70%	-7.40%	-5.40%	-2.30%	-0.60%	-0.80%
	KFX	-14.80%	-1.80%	-89.80%	0.00%	0.00%	-40.70%
	KFY	21.50%	-71.90%	29.90%	4.40%	-0.40%	8.60%
	KMZ	113.20%	433.30%	117.90%	16.60%	-95.50%	-20.40%
J=0.8	KT	11.50%	-11.90%	15.20%	-2.00%	-8.80%	-9.50%
	KQ	10.20%	-14.70%	11.10%	-7.50%	-6.50%	-4.70%
	KFX	935.10%	-8.00%	303.40%	79.30%	-5.70%	5.30%
	KFY	38.20%	124.80%	75.30%	14.50%	148.20%	4.00%
	KMZ	-23.40%	167.60%	64.60%	2.40%	198.10%	5.90%

Table 9: Percentage difference between Measurements and Predictions of pod performance coefficients using steady and unsteady simulation conditions for pusher Pod in difference azimuthing conditions.

		Steady			Unsteady		
		30	0	-30	30	0	-30
J=0.2	KT	-1.3%	-2.6%	1.4%	-3.2%	-0.9%	-0.8%
	KQ	-9.1%	-8.1%	-1.1%	-1.5%	-4.6%	-2.1%
	KFX	-20.9%	2.1%	9.8%	-2.3%	1.5%	9.9%
	KFY	20.6%	118.9%	30.3%	1.1%	120.8%	-3.8%
	KMZ	-35.1%	96.1%	-21.9%	-5.2%	-33.4%	-3.1%
J=0.5	KT	1.0%	-8.0%	0.3%	-0.8%	-4.2%	-2.5%
	KQ	-14.0%	-14.0%	1.5%	-2.5%	-4.2%	1.5%
	KFX	-18.0%	-3.7%	81.1%	-0.5%	0.4%	14.8%
	KFY	8.0%	60.5%	17.7%	-6.4%	26.3%	-10.5%
	KMZ	-62.5%	79.3%	-32.6%	-3.4%	27.7%	-11.3%
J=0.8	KT	1.9%	-8.6%	-10.7%	1.6%	-2.0%	-4.8%
	KQ	-25.4%	-16.6%	-9.5%	-4.2%	-5.4%	2.9%
	KFX	-161.8%	-18.0%	-113.1%	27.8%	-8.8%	9.1%
	KFY	-17.4%	-161.3%	-6.9%	-6.9%	-75.9%	-12.5%
	KMZ	-94.9%	52.3%	-24.2%	-24.6%	12.4%	-24.3%

4.5 (a) Propeller-Pod-Strut Interactions

Further analysis has been carried out on the pressure and velocity distributions on the pod as obtained from the simulations. The pressure distribution on the pod-strut body in straight-ahead puller configuration, Figure 27, shows slightly higher pressure on the left side of the strut, when looking toward the propeller. The figure also presents the pressure distribution on the pressure side of the pod-strut body for positive and negative and moderate azimuthing angles ($\pm 30^\circ$) for the puller and pusher configurations. The comparative figures clearly demonstrate the effect of sign of azimuthing angle on the pressure distribution of pod-strut body.

The velocity distribution around the pod-strut-propeller on a horizontal plane through propeller centre for each of the pod configurations and propeller loading conditions at static azimuthing angle of $\pm 30^\circ$ are presented in Figure 28. These were obtained using unsteady state simulations. The flow separation and propeller-pod interaction are apparent for $\pm 30^\circ$. The flow separation is predicted well, which may not be captured accurately by the steady state approach used. The effect of propeller rotation direction for the positive and negative azimuthing angle is also evident in the unsteady simulations.

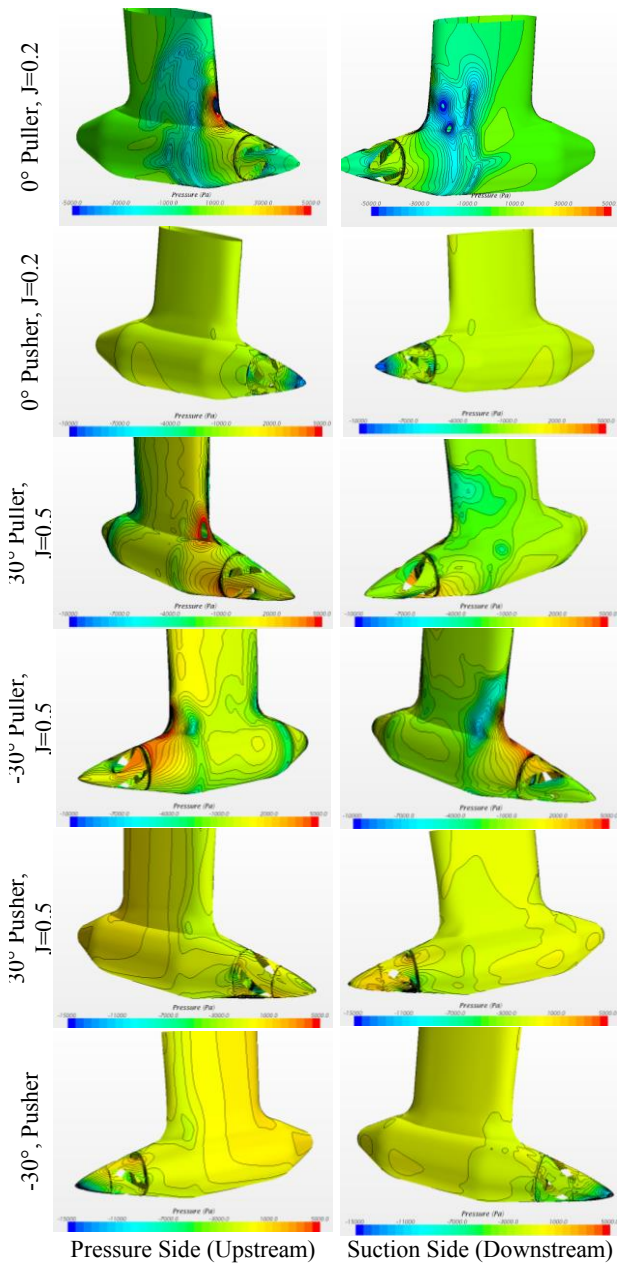


Figure 27 – The pressure distribution on pod-strut body at different azimuthing and loading conditions for pusher and puller configurations

5. CONCLUDING REMARKS

The hydrodynamic performance of podded propulsors is investigated through numerical simulations at multiple configurations, loading conditions and azimuthing angles. A finite volume based Reynolds-Averaged Navier Stokes (RANS) solver is used to predict the propulsive performance of the single pod unit at multiple practical conditions.

Steady and unsteady state simulations are completed for all cases. There is a good agreement between the steady state simulation and the experimental results when the azimuthing angle was between 0 to $\pm 30^\circ$. A significant improvement in predicting the thrust and torque was noticed in the results of the unsteady state simulations as

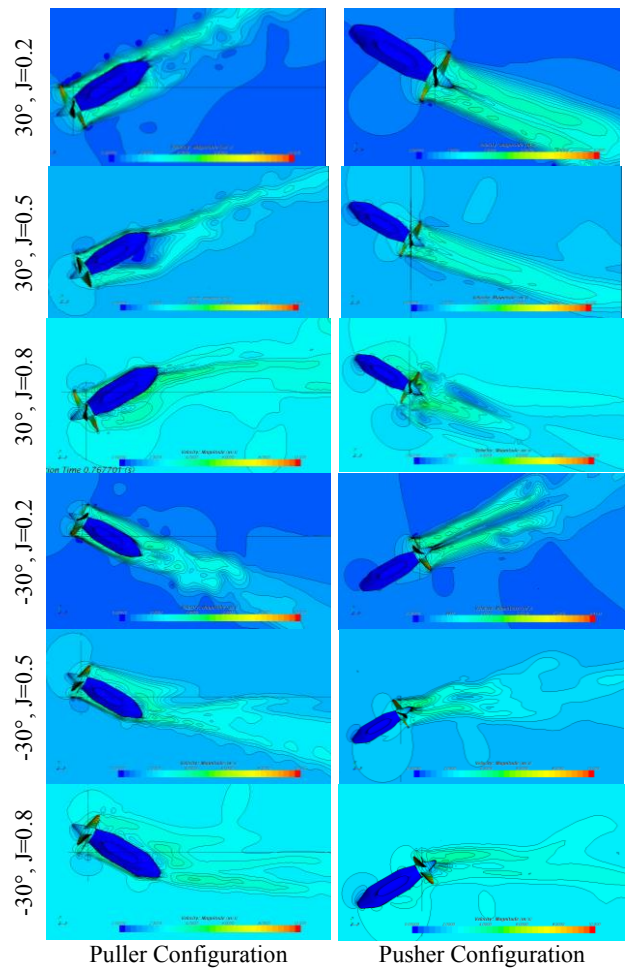


Figure 28 – The velocity flow field around the pod, strut, and propeller for puller and pusher configurations at multiple azimuthing angles, loading conditions and pod configurations.

compared to the steady ones, especially for the $\pm 30^\circ$ azimuthing conditions.

Both the measurements and the RANS predictions showed that the axial force coefficient decreased for both azimuthing directions but the reduction was visibly stronger for negative azimuthing angles. The side force and steering moment coefficients change approximately linearly with the change of azimuthing angle in the moderate range of azimuthing angles of $\pm 30^\circ$. The predicted results acquired by the time accurate simulations captured these phenomena more accurately than the steady state ones.

It is observed that performing the simulations in unsteady state setup takes approximately three times higher than in

steady state setup for a similar simulation. Considering the improvement in accuracy of the predictions, it may be logical to use the unsteady state setup for simulations to predict performance of pod unit in the advanced design stages; steady state simulations may be accurate enough in early design stage.

The authors believe the simulation techniques presented in the paper will enhance the numerical simulation capability of the relevant research community to capture most of the dynamics of podded propulsion systems.

6. ACKNOWLEDGEMENTS

The authors thank Oceanic Consulting Corporation for their financial and other support for the numerical research program. The simulation work was carried out at Oceanic as part of a project which was supported by the Atlantic Innovation Fund administered by Atlantic Canada Opportunities Agency. This support is also gratefully acknowledged.

7. REFERENCES

1. CARLTON, J. S. 2002, Podded Propulsors: some design and service experience, *The Motor Ship Marine Propulsion Conference, Copenhagen, Denmark, April 9-10, 2002*, 7p.
2. PAKASTE, K. LAUKIA, M. WILHELMSON, 1999, Experience with Azipod® Propulsion Systems on Board Marine Vessels, *ABB Review, Issue 2*, 12p.
3. ISLAM, M. F. 2009, Performance study of podded propulsors with varied geometry and azimuthing conditions, *Doctoral Dissertation, Memorial University of Newfoundland, St. John's, NL, Canada*, 245p.
4. SZANTYR, J. A. 2001a, Hydrodynamic model experiments with pod propulsor, *International symposium of ship propulsion (Lavrentiev Lectures), State Marine Technical University, St. Petersburg, Russia*, pp. 95-104.
5. SZANTYR, J. A. 2001b, Hydrodynamic model experiments with pod propulsor, *Oceanic Engineering International, Vol. 5, No.2*, pp. 95-103.
6. GRYGOROWICZ, M. AND SZANTYR, J. A. 2004, Open water experiments with two pods propulsor models, *In Proceedings of the 1st International Conference on Technological Advances in Podded Propulsion, Newcastle University, UK, April*, pp. 357-370.
7. WOODWARD, M. D. 2006, Steady control and response of pod driven ships, *PhD thesis, School of Marine Science and Technology, University of Newcastle-upon-Tyne*, 255p.
8. HEINKE, H. J. 2004, Investigation about the forces and moments at podded drives, *In Proceedings of the 1st International Conference on Technological Advances in Podded Propulsion, Newcastle University, UK, April*, pp. 305-320.
9. STETTLER, J. W. 2004, Steady and unsteady dynamics of an azimuthing podded propulsor related to vehicle maneuvering, *PhD thesis, Massachusetts Institute of Technology*, 187p.
10. REICHEL, M. 2007, Manoeuvring forces on azimuthing podded propulsor model, *Polish Maritime Research, Versita, ISSN: 1233-2585, Vol. 14, No. 2*, pp 3-8.
11. WANG, J. 2007, Prediction of propeller performance on a model podded propulsor in ice (propeller-ice interaction), *PhD thesis, Faculty of Engineering and Applied Science, Memorial University of Newfoundland, Canada*, 251p.
12. ISLAM, M. F. VEITCH, B. AKINTURK, A. BOSE, N. and LIU, P. 2008, Performance study of podded propulsor in static azimuthing conditions, *International Shipbuilding Progress, Vol. 56, No 3-4*, pp. 135-157.
13. AKINTURK, A. ISLAM, M. F. VEITCH, B. 2012, Performance Dynamic Azimuthing Podded Propulsor, *International Shipbuilding Progress, Vol. 59*, pp. 83-106.
14. LIU, P., ISLAM, M., VEITCH, B., 2009. Unsteady hydromechanics of a steering podded propeller unit, *J. Ocean Engineering, 36(12-13)*, pp.1003-1014.
15. AMINI, H., SILEO, L., STEEN S., 2012. Numerical calculations of propeller shaft loads on azimuth propulsors in oblique inflow, *J. Marine Science and Technology , 17(4)*, pp.403-421.
16. SANCHEZ-CAJA, A., RAUTAHEIMO, P., SIIKONEN, T., 1999. Computation of the incompressible viscous flow around a tractor thruster using a sliding-mesh technique, *In Proceedings of 7th International Conference on Numerical Ship Hydrodynamics, France*.
17. OHASHI, K., HINO, T., 2004. Numerical simulations of the flows around a ship with podded propulsor, *In First International Conference on Technological Advances in Podded Propulsion, University of Newcastle, UK*, pp. 211-221.
18. JUNGLEWITZ, A., EL MOCTAR, O.M., 2004. Numerical analysis of the steering capabilities of a podded drive, *Ship Technology Research, Schiffstechnik, Vol. 51(3)*, pp.134-145
19. GUO CHUN-YU, MA NING, YANG CHEN-JUN, 2009. Numerical simulation of a podded propulsor in viscous flow, *J. of Hydrodynamics, 21(1)*, pp.71-76
20. ARIKAN Y., DOĞRUL A., ÇELİK F., 2012. Performance Analysis and Investigation of the Slipstream Flow of podded propeller, *Brodogradnja, 63(3)*, pp.226-233
21. SHAMSI, R., GHASSEMI, H., 2013. Hydrodynamic analysis of puller and pusher of

- azipod at various yaw angles, *J. Engineering for the Maritime Environment*, accepted
22. ITTC – Recommended Procedures, 2002, Propulsion, Performance - *Podded Propeller Tests and Extrapolation*, 7.5- 02-03-01.3, Revision 00.
 23. MEWIS, F. 2001, The efficiency of pod propulsion, *HADMAR 2001, Bulgaria, October*, 7p.
 24. WILCOX, D.C., 1998. Turbulence modeling for CFD, 2nd edition, *DCW Industries, Inc., La Canada, California*.
 25. MENTER, F.R. 1994. Two-equation eddy-viscosity turbulence modeling for engineering applications, *AIAA Journal*, 32(8), pp. 1598-1605.
 26. FERZIGER, J.H. and PERIC, M. 2002, ‘*Computational Methods for Fluid Dynamics*’,
 27. ACHKINADZE, A. S. BERG, A. KRASILNIKOV, V. and, STEPONOV, I. E. 2003, Numerical Analysis of Podded and Steering Systems using a Velocity Based Source Boundary Element Method with Modified Trailing Edge, *Proc of the Propellers/Shafting 2003 Symposium, SNAME, VA USE Sept 17-18, 2003*, 22p.
 28. KRASILNIKOV, V. ZHANG, Z. HONG, F. 2009, Analysis of Unsteady Propeller Blade Forces by RANS, *First International Symposium of Marine Propulsors, SMP-09, Trondheim, Norway, June 2-009*, 11p.